



Short communication

Multifunctional and multi-site interfacial buffer layer for efficient and stable perovskite solar cells



Pengyu Su^{a,b,c}, Huan Bi^{d,*}, Du Ran^a, Li Liu^{e,*}, Wenjing Hou^g, Guangzhao Wang^{a,b,c}, Wenbing Shi^{f,*}

^a School of Electronic Information Engineering, Yangtze Normal University, No. 16, Juxian Avenue, Fuling District, Chongqing 408100, PR China

^b Department of Applied Physics, Chongqing University, No. 174, Main Street, Shapingba District, Chongqing 400044, PR China

^c Longxin Industry Co., Ltd, Chongqing 400000, PR China

^d Graduate School of Informatics and Engineering, The University of Electro-Communications, 1-5-1 Chofugaoka, Chofu, Tokyo 182-8585, Japan

^e Joint Laboratory for Extreme Conditions Matter Properties, School of Mathematics and Physics, Southwest University of Science and Technology, Mianyang 621010, PR China

^f Chongqing Key Laboratory of Inorganic Special Functional Materials, College of Chemistry and Chemical Engineering, Yangtze Normal University, No. 16, Juxian Avenue, Fuling District, Chongqing 408100, PR China

^g Institute of Molecular Science, Key Laboratory of Materials for Energy Conversion and Storage of Shanxi Province, Shanxi University, Taiyuan 030006, PR China

ARTICLE INFO

ABSTRACT

Keywords:

Perovskite solar cells
Multi-site multifunctional molecule
Buried interface
 SnO_2
Stress relief
Defect passivation

Perovskite solar cells (PSCs) have achieved significant success in power conversion efficiency (PCE) and stability. However, interfacial recombination and film defects still hinder the improvement of PSCs efficiency. In this study, we propose a novel interfacial buffer layer material called Ethyl p-nitrobenzoate (EPN) to enhance device performance and stability. Our results demonstrate that introducing EPN improves the film's quality, reduces defect density, relieves interfacial stress, and significantly suppresses nonradiative recombination at the interface. Density functional theory (DFT) calculations confirm that EPN can effectively passivate defects in the perovskite and SnO_2 films due to its multifunctionality. Finally, we achieved a high PCE of 23.16% for the target device while significantly enhancing device stability compared to the control. This work provides new insights into the development of multifunctional multi-site interfacial buffer layers for high-performance PSCs.

1. Introduction

As the most promising third-generation photovoltaic device, perovskite solar cells (PSCs) have achieved a certified efficiency of 25.7% since they were first reported in 2009, comparable to silicon-based solar cells, a treasure in the photovoltaic market [1,2]. However, poor film quality, severe interfacial nonradiative recombination, and interfacial stress hinder further device efficiency breakthroughs [3–6]. At the same time, these problems also bring about the loss of device stability [4,7,8]. Therefore, how to solve the above issues is the key to realizing the commercialization of PSCs.

Tin dioxide (SnO_2) has demonstrated its superior performance as a promising electron transport material (ETL), and most of the current high-efficiency PSCs are based on SnO_2 as ETL [1,9–14]. The preparation of the SnO_2 layer is generally made by a spin-coating process, which causes defects in the film, especially oxygen vacancy defects that can

become nonradiative recombination sites [15–18]. Therefore, how to reduce oxygen vacancy defects and further improve the quality of SnO_2 film is very important. The more common strategies to improve the quality of SnO_2 film are additive strategy and interface modification strategy [19–21]. For example, Sun and his group used biguanide hydrochloride as a buffer layer to modify the buried interface [22]. The results show that the buffer layer significantly improves the electron extraction at the interface and helps to obtain better-quality perovskite films. At the same time, the energy levels are more matched, the open circuit voltage of the final device is as high as 1.19 V, and the device efficiency of more than 24% is obtained simultaneously. We tried to use Girard's Reagent T as an additive of SnO_2 to improve the performance of the device by improving the properties of SnO_2 . We found that the SnO_2 solution introduced with the additive improves the stability and makes obtaining high-quality perovskite films easier [23]. The final device achieved an efficiency of over 21%. In addition, while considering the

* Corresponding authors.

E-mail addresses: hbi.trans.sci@uec.ac.jp (H. Bi), liuli_phy@swust.edu.cn (L. Liu), swb@yznu.edu.cn (W. Shi).

reduction of nonradiative recombination sites, we also expect to improve the energy level arrangement, which will also benefit the transport of carriers [24–26].

Perovskite film quality is another factor that affects device efficiency and stability [27]. As reported, water and oxygen accelerate device failure by attacking defect sites in the film [28,29]. Some strategies have been proposed to improve perovskite film quality, such as additive engineering, solution addition, interface engineering, and antisolvent engineer [30–33]. Interface engineering is an effective strategy. On the one hand, by changing the substrate's properties, the film's quality can be significantly improved [34–36]. On the other hand, substrate changes can release the stress of the film, thereby delaying the device's failure [37,38]. Moreover, interface engineering strengthens the connection between functional layers, thereby preventing device failure. Based on the above, it is urgent to find suitable interface modification materials to improve the performance and stability of devices.

Here, we developed a novel interfacial buffer material named Ethyl p-nitrobenzoate (EPN) to improve the interfacial connection between the electron transport and perovskite layers. Experiments and theoretical calculations prove that EPN can simultaneously generate a strong chemical interaction between the electron transport layer and the perovskite, which can effectively passivate the film defects and enhance the interfacial link. Meanwhile, the flexible EPN can also effectively

release interfacial stress. In addition, interfacial nonradiative recombination is also significantly suppressed due to the addition of EPN. Finally, the PSCs introduced into the buffer layer achieved an efficiency of 23.16%. Furthermore, the stability of the device (Light, humidity, and temperature conditions) has been improved.

2. Results and discussion

The structure of the device used in this work is shown in Fig. 1a. In order to improve the performance of the device with the SnO_2 as ETL, Ethyl p-nitrobenzoate (EPN) was introduced to modify the interface between SnO_2 and perovskite ($\text{Rb}_{0.02}(\text{FA}_{0.95}\text{Cs}_{0.05})_{0.98}\text{PbI}_{2.91}\text{Br}_{0.03}\text{Cl}_{0.06}$), as presented in Fig. 1b. The molecule structure shows in Fig. S1. First, the carbonyl group (-C = O) is expected to coordinate with Pb^{2+} or Sn^{4+} through the electrostatic attraction between -C = O and Pb^{2+} or Sn^{4+} , thereby passivating cation defects at the SnO_2 /perovskite interface (such as undercoordinated Pb^{2+} (from perovskite thin film) or under-coordinated Sn^{4+} (from SnO_2 film)), thereby improving the quality of each functional layer. Secondly, nitro (-NO₂), although rarely noticed as a typical electron-withdrawing solid group, is also expected to interact with undercoordinated Pb^{2+} through a coordination reaction [39–42]. Gao and his coauthor reported a simple passivating molecule, 4-nitrophthalonitrile (4NPN), with σ-π accepting

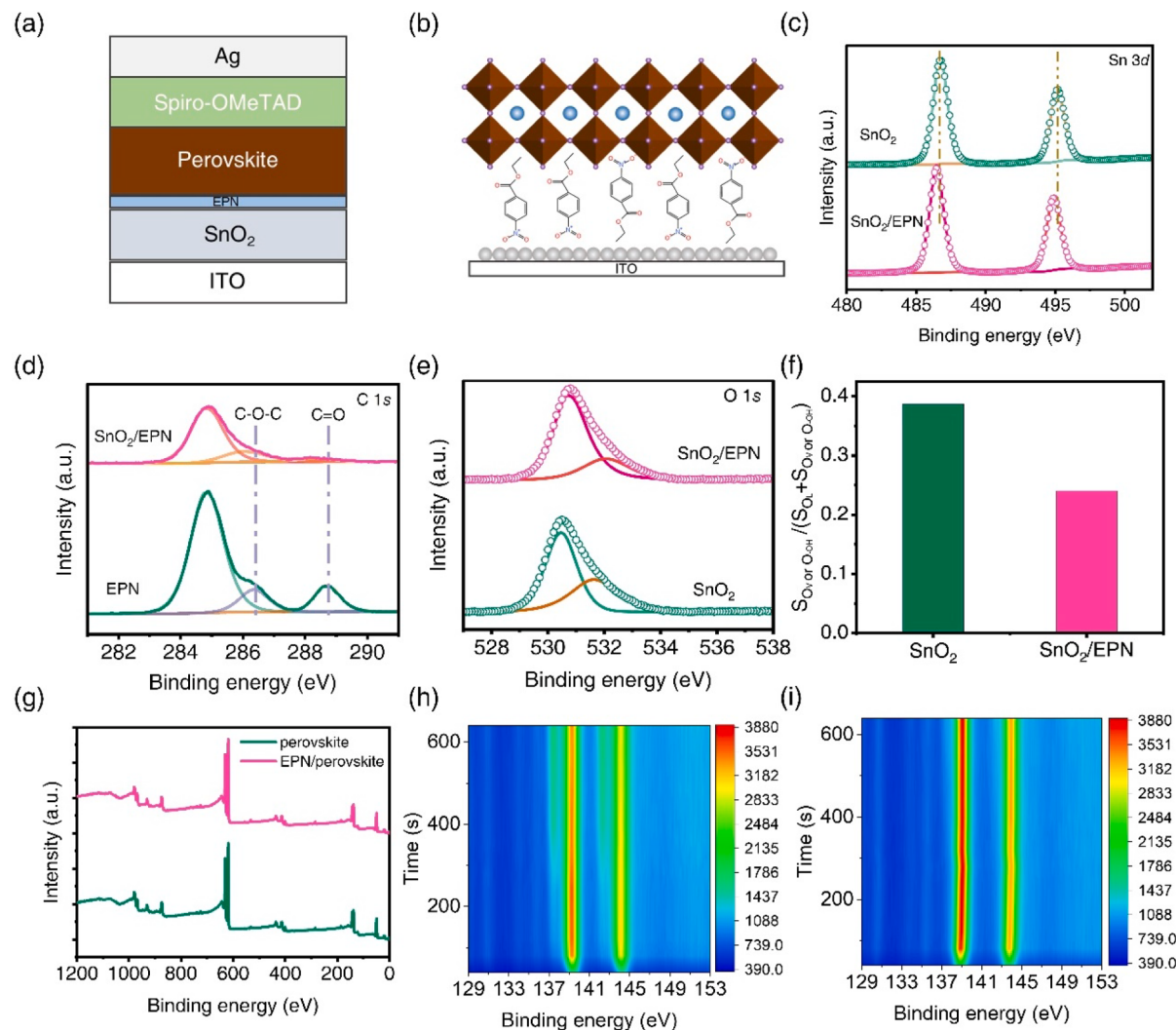


Fig. 1. (a) Schematic illustration of the device structure of the PSCs used in this work. (b) Schematic illustration of the formation of EPN on the SnO_2 layer. XPS (c) Sn 3d (d) C 1 s and (e) O 1 s core-level spectra of SnO_2 , EPN, or SnO_2/EPN films. (f) Oxygen vacancy ratio. (g) Full XPS spectra of the perovskite and EPN/perovskite films. Depth-dependence of the XPS Pb 4f of the (h) ITO/ SnO_2 /perovskite and (i) ITO/ SnO_2/EPN /perovskite. Y axis represents etching time.

nitro ($-NO_2$) and cyano groups ($-CN$), was employed to passivate the charged defects in perovskites. The addition of electron-deficient 4NPN into the perovskite layer of PSCs could enhance V_{OC} and the FF, leading to high PCE over 22% and improved environmental stability. These improvements were attributed to the effective passivation of the defects in the perovskite film by the strongly polarized nitro/cyano groups [43]. Third, long alkyl chains have also been beneficial in relieving interfacial stress, and improving the growth quality of perovskite films [44–47]. As interfacial modifiers, organic compounds have been widely demonstrated to passivate the quality of perovskite films while enhancing interfacial connectivity. EDS was used to uncover the EPN indeed existence on the SnO_2 layer. As shown in Fig. S2, the N element, as a characteristic element of EPN, can be detected on the surface of SnO_2 , which proves that EPN exists at the SnO_2 interface. X-ray photoelectron spectroscopy (XPS) was first used to uncover the chemical interaction between SnO_2 and EPN. As exhibited in Fig. S3 and Fig. 1c, the binding energies of $Sn\ 3d_{3/2}$ (495.22 eV) and $Sn\ 3d_{5/2}$ (486.77 eV) peaks of SnO_2 were shifted to the lower binding energy of 494.88 and 486.43 eV after EPN modification, respectively, indicating that the electron cloud density around Sn increases [22]. This increasing electron cloud density can lead to a decrease in the valence state of Sn, and the extra electrons originate from the $-X = O$ ($X = N$ or C) of EPN, a typical electron donor, which suggest that the strong chemical interaction between EPN and SnO_2 . Fig. 1d shows the C 1 s orbital binding energies of EPN and SnO_2/EPN , respectively. The apparent shift occurs while EPN is deposited on SnO_2 , indicating a chemical interaction between SnO_2 and EPN. In addition, an asymmetric spectrum profile can be observed in both bare SnO_2 and EPN-modified SnO_2 films of the O 1 s core-level spectrum (Fig. 1e). The O 1 s peak of both samples deconvoluted into two peaks. Among them, the lower binding energy peak can attribute to the $Sn-O-Sn$ (lattice oxygen, O_L) in SnO_2 , and the higher binding energy peak is

assigned to oxygen vacancies (O_V) or surface-absorbed hydroxyl (O_{OH}) [27]. The peak area ratio of O_V or $-OH$ (S_{OV} or S_{OH}) was estimated by the formula of $S_{OV} \text{ or } -OH = S_{OV} \text{ or } -OH / (S_{OL} + S_{OV} \text{ or } -OH)$, where S_{OV} or S_{OH} and S_{OL} stand for the peak area of O_V or $-OH$ and O_L , respectively. The S_{OV} or S_{OH} of SnO_2 modified with EPN was calculated to be 0.24, which was lower than 0.38 of the bare SnO_2 film (Fig. 1f). This result suggests that the oxygen vacancies of the SnO_2 can be effectively filled by EPN, which is expected to improve the performance of the device. The depth-dependent XPS of Pb 4f was also carried out to prove the chemical interaction between EPN and perovskite. As presented in Fig. 1g-i, the binding energies of bare perovskite at 138.6 eV and 143.5 correspond to $Pb\ 4f_{7/2}$ and $Pb\ 4f_{5/2}$, respectively. While the peaks shift by 150 meV to the lower binding energy after EPN is modified, which proves that the Pb^{2+} got the electrons from EPN and the undercoordinated Pb^{2+} can be effectively passivated [22]. Besides, two binding energy peaks at 137.12 eV and 142.3 eV were observed for the control sample correspond to metallic Pb [48]. Noticeably the metallic Pb peaks were associated with cation and iodide vacancies in the perovskite film, while the EPN treatment could significantly suppress them. In a word, there is a strong chemical interaction between EPN and both SnO_2 and perovskite, which can effectively passivate the vacancies and defects existing in the film, thereby improving the film quality.

First-principles density functional theory (DFT) calculations were performed further to investigate the interaction between EPN and SnO_2 or perovskite. The most stable termination of the SnO_2 (110) surface was chosen according to the previous study [49,50]. A charge density difference map was carried out and displayed in Fig. 2a and 2b. Here, two different contact modes of EPN (-C = O or -N = O) are constructed to contact the SnO_2 surface with oxygen vacancies. It is obvious that significant charge transfer occurs at the interface with both contact modes, indicating that EPN can strongly chemically interact with SnO_2 at

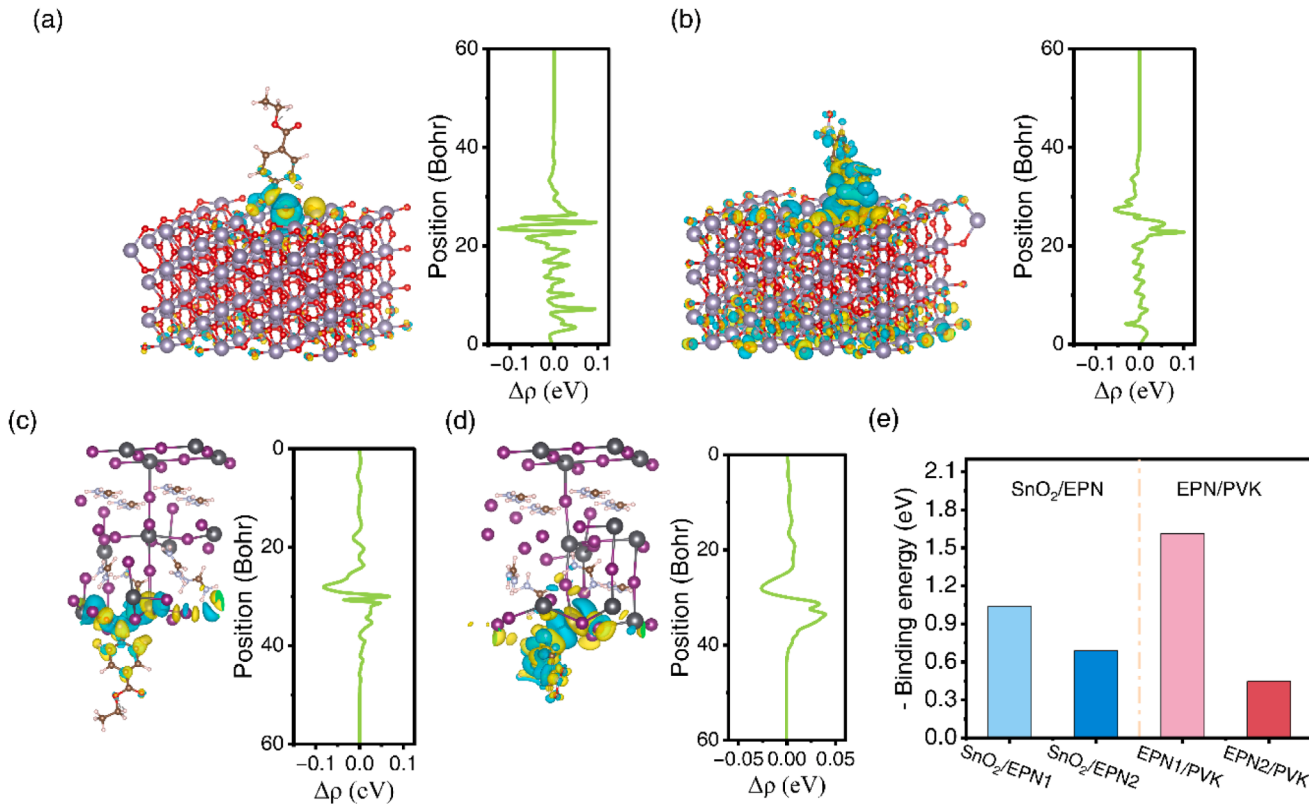


Fig. 2. The differential charge densities of (a) SnO_2/EPN linked with $-NOO$, (b) SnO_2/EPN linked with $-C=O$ and $C-O-C$. (c) and (d) show the differential charge densities of EPN/perovskite with $-NOO$ and $-C=O/C-O-C$ linked, respectively. Z on the y-axis in (a)-(d) represents the length of the vacuum slab and an example of SnO_2/EPN or EPN/perovskite slab is shown to indicate the corresponding position in the Z direction. (e) the binding energy between the SnO_2/EPN and EPN/perovskite, where EPN1 stands for the $-NOO$ linked and the EPN2 stands for the $-C=O/C-O-C$ linked.

multiple sites. The charge density map mapped on the Z-axis makes this chemical transfer more apparent (right of Fig. 2a and 2b). Noticeable charge density fluctuations can be seen at the interface (SnO_2/EPN) through both contact modes, which shows that this charge transfer is very clear at the interface. Furthermore, the chemical interaction between EPN and perovskite has also been studied. As shown in Fig. 2c and 2d, we still construct two different contact models for evaluating the chemical interaction between EPN and perovskite. There is a substantial charge transfer at the interface of EPN and perovskite, which makes the chemical interaction between EPN and perovskite occur. In a word, the charge density difference maps reveal the strong chemical interaction between EPN (multiple sites) and SnO_2 or perovskite, corresponding to the result of XPS.

Furthermore, the binding energy (E_b) of the EPN (different contact mode) and SnO_2 or perovskite were calculated via the formula of $E_b = E(\text{EPN}) + E(\text{SnO}_2 \text{ or perovskite}) - E(\text{SnO}_2/\text{EPN} \text{ or EPN/perovskite})$, where $E(\text{EPN})$, $E(\text{SnO}_2 \text{ or perovskite})$ and $E(\text{SnO}_2/\text{EPN} \text{ or EPN/perovskite})$

stand for the total energies of EPN, SnO_2 or perovskite surface and their heterojunction systems, respectively [51]. As shown in Fig. 2e, the E_b between SnO_2 and EPN are 1.040 eV and 0.688 eV, respectively, and 1.614 eV and 0.450 eV between EPN and perovskite. This result proves that all EPN (EPN1 or EPN2) contact modes can form a stable system with SnO_2 and perovskite.

Such a strong chemical interaction encourages us to uncover the effect of EPN on the perovskite film. UV-Vis absorption spectra of the perovskite film with or without EPN modification were measured and exhibited in Fig. S4. It can be observed that the target film exhibits a slight increase in absorbance compared to the control one. In addition, the bandgap (E_g) of the perovskite film was also calculated via the Tauc plot (Fig. S5). All samples show $E_g = 1.55$ eV. In addition, the perovskite solution contact angle was further carried out. As shown in Fig. S6, after EPN was introduced, the contact angle was decreased from 16° (ITO/ SnO_2) to 9° (ITO/ SnO_2/EPN), which is expected to improve the perovskite film morphology. Then, the morphology of the perovskite film

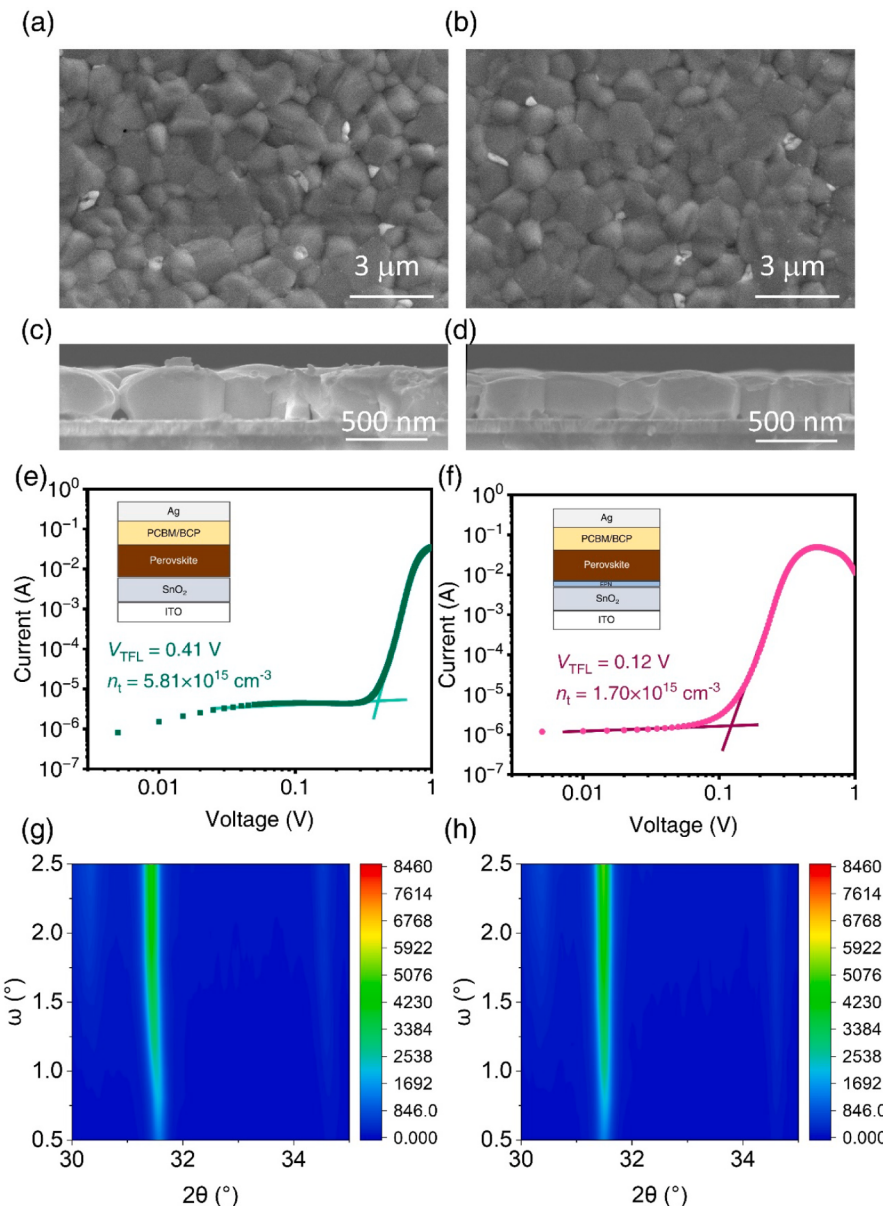


Fig. 3. Top-view SEM images of the (a) control and (b) target perovskite films. Cross-section SEM of the (c) control and (d) target perovskite films. Dark I-V curves of the device with the structure of (e) ITO/ SnO_2 /perovskite/PCBM/BCP/Ag and (f) ITO/ SnO_2 /EPN/perovskite/PCBM/BCP/Ag. Depth-dependent GIXRD patterns of the perovskite films with the structure of (g) ITO/ SnO_2 /perovskite and (h) ITO/ SnO_2 /EPN/perovskite.

deposited on ITO/SnO₂ or ITO/SnO₂/EPN was studied by scanning electron microscopy (SEM), shown in Fig. 3a and 3b. It is obvious that a larger grain size was obtained with EPN modified compared with the control sample (Fig. S7). As revealed by cross-sectional SEM images in Fig. 3c and 3d, clear pinholes can be observed in the perovskite film deposited on unmodified SnO₂ film. We investigated the crystallization process for the perovskite films without and with EPN during annealing by UV-vis absorption spectra. The stronger absorption was found at the same annealing time for the perovskite film with EPN compared to the control film (Fig. S8). Meanwhile, during the initial annealing, the control device showed a strong UV absorption signal, while the target device did not. This result indicated that EPN would delay the crystallization, which is beneficial to increase the grain size.

Photoluminescence (PL) and time-resolved PL (TRPL) spectra were employed first. As shown in Fig. S9, the target perovskite film (glass/EPN/perovskite) shows a higher PL intensity than the control perovskite film (glass/perovskite). Perovskite film carrier lifetime was further assessed by the TRPL (Fig. S10) with the structure of glass/with or without EPN/perovskite. TRPL curve can be fitted by the double exponential decay equation of $I(t) = I_0 + A_1 \exp(-t/\tau_1) + A_2 \exp(-t/\tau_2)$, where A_1 and A_2 represent the decay amplitude of fast and slow decay process, respectively. τ_1 and τ_2 are the fast and slow decay time constants, respectively [27]. The average carrier lifetime (τ_{ave}) was calculated by using the equation of $\tau_{ave} = (A_1\tau_1^2 + A_2\tau_2^2)/(A_1\tau_1 + A_2\tau_2)$. The corresponding fitted data are given in Table S1. The target perovskite film exhibited significantly enhanced carrier lifetimes ($\tau_{ave} = 228.10$ ns) than the control ($\tau_{ave} = 122.59$ ns). Space charge limited current (SCLC) technology was further employed to calculate the defect densities of perovskite films quantitatively. Fig. 3e-f exhibit the typical dark current–voltage ($I-V$) curves of the electron-only devices with ITO/SnO₂/perovskite/PCBM/BCP/Ag structure and ITO/SnO₂/EPN/perovskite/PCBM/BCP/Ag. The trap density calculates by the equation of $n_t =$

$(2\varepsilon\varepsilon_0 V_{TFL})/(eL^2)$, [52] where ε_0 is the vacuum dielectric constant, ε is the dielectric constant of the perovskite, V_{TFL} is the trap-filled limit voltage obtained by fitting dark $I-V$ curves, e is the elementary charge, and L is the thickness film of the perovskite. The defect density of the control perovskite film was estimated to be $5.81 \times 10^{15} \text{ cm}^{-3}$, much higher than the $1.70 \times 10^{15} \text{ cm}^{-3}$ of the target perovskite film.

To better understand the mechanisms of the significant optimized film quality by simple interface modification, depth-dependent grazing incident X-ray diffraction (GIXRD) was employed to study the stress situation at the interface (SnO₂/perovskite) [22,27]. It is well known that the existence of interfacial stress can result in film cracking and increase the probability of pinholes. Simultaneously, the interfacial stress also affects the crystallization properties of the film, thereby increasing the defects. Different incident angles (ω) were carried out according to our previous work [27]. With the increase of ω , deeper thin-film signals can be collected. As shown in Fig. S11, and 3 g-h, the control film's peak position significantly shifts with the ω increasing while the negligible shifted peak position in EPN passivated perovskite films was observed. According to Bragg's Law, we evaluated the interplanar spacing (d -spacing) in the vertical direction of the perovskite film. Here, we selected high-angle diffraction peaks according to reports [53–55]. As shown in Fig. S12, for the control perovskite film, as ω increases, d also increases, while for the target film, d does not significantly increase as ω increases. This result indicates residual tensile stress in the control film, and the stress of the target film is almost released. Our previous work has proved that the passivation of undercoordinated Pb²⁺ can effectively release stress [26,27]. Moreover, long chains on EPN are also beneficial for stress release [46,56,57].

Then, some effective characterization techniques were used to investigate deep insights into the interfacial carrier transport with or without EPN modification. PL and TRPL were first performed and shown in Fig. 4a and S13. The PL intensity of the control film with an ITO/

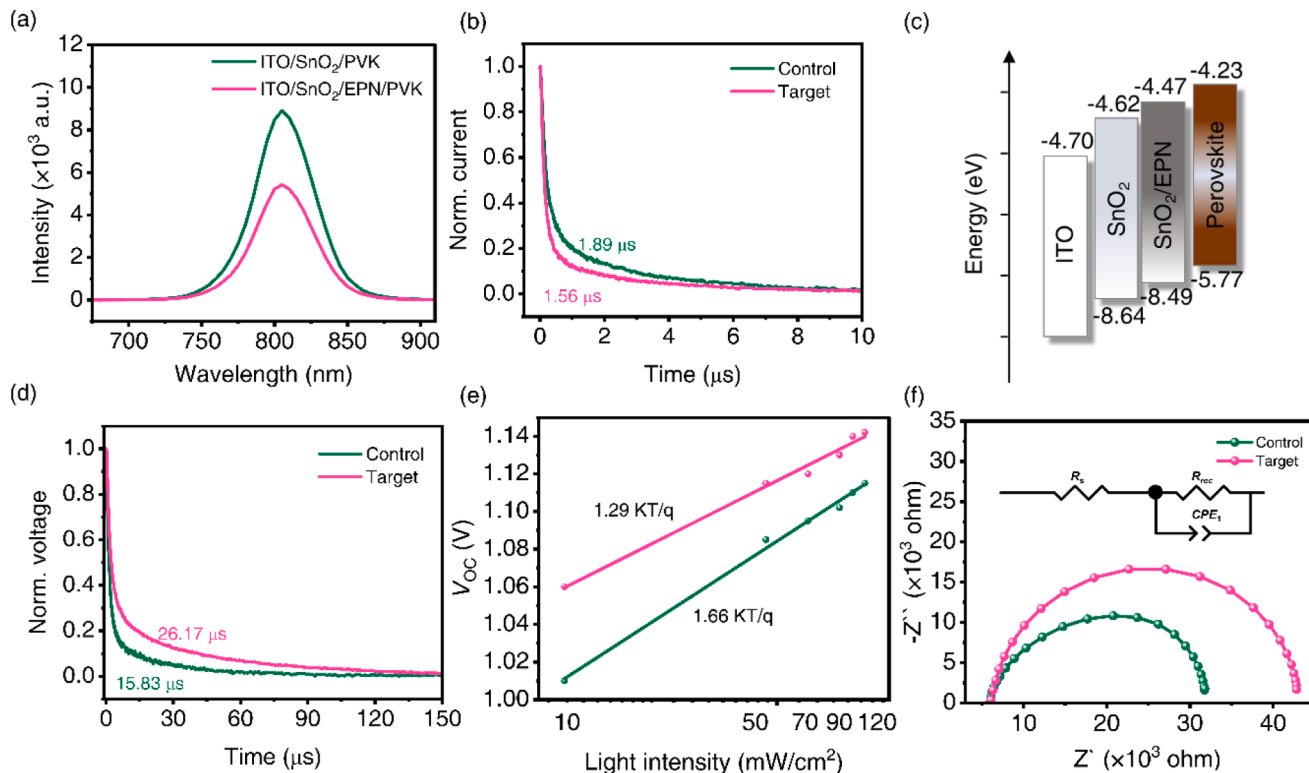


Fig. 4. (a) PL of the device with ITO/SnO₂/perovskite structure and ITO/SnO₂/EPN/perovskite. (b) TPC curves of the device with or without EPN modification (ITO/SnO₂/EPN/perovskite/Spiro-OMeTAD/Ag). (c) Energy level diagram of device components in this study. (d) TPV curves of the device with or without EPN modification (ITO/SnO₂/EPN/perovskite/Spiro-OMeTAD/Ag). (e) V_{OC} depends on light intensity for the devices with or without EPN modification. (f) Nyquist plots of the PSCs based on SnO₂ and SnO₂/EPN were obtained with a bias of V_{OC} under the dark. The equivalent circuit used for fitting is illustrated in the inset.

SnO_2 /perovskite structure was lower than that of the target film with an ITO/ SnO_2 /EPN/perovskite structure, which means that the carrier transport improved while EPN was introduced. TRPL results (Table S2) also indicate that the carrier transport of the target film (6.43 ns) is improved compared to the control (10.80 ns). Transient current (TPC) was further used to consider the charge transport with EPN modified. As shown in Fig. 4b, the carrier lifetimes reduced from 1.89 μs to 1.56 μs after EPN was introduced to the interface of SnO_2 /perovskite, which proves that the carrier transfer at the interface indeed improved when EPN acts as a buffer layer. Mott-Schottky curves of the control and target devices were carried out to determine the source for carrier transport improvement. Obviously, built-in potential (V_{bi}) significantly increased after EPN treatment, as shown in Fig. S14. Due to the driving force of the device carriers during working coming from the potential difference, a larger V_{bi} is more conducive to transporting carriers. Meanwhile, a more matchable energy level also benefits carrier transfer. Here, we evaluated the energy level with or without EPN modification. As shown in Fig. S15 and Fig. 4c, the valence band maximum (VBM) values of SnO_2 and SnO_2 /EPN were -8.64 eV and -8.49 eV, respectively. Furthermore, the conductive band minimum (CBM) was -4.62 eV and -4.47 eV. The bandgap of the SnO_2 was obtained from previous work [49]. As reported, about 0.2–0.3 eV energy offset is more beneficial for facilitating carrier transfer [58,59]. Intensity-modulated photocurrent spectroscopy (IMPS) and intensity-modulated photovoltage spectroscopy (IMVS) were conducted to calculate the charge-collection efficiency (η_{cc}) with the formula of $\eta_{\text{cc}} = 1 - \tau_{\text{tr}}/\tau_{\text{rec}}$. Furthermore, the electron recombination lifetime (τ_{rec}) and electron transport lifetime (τ_{tr}) can be calculated by the following equations: $\tau_{\text{rec}} = 1/(2^* \pi^* f_{\text{IMPS}})$ and $\tau_{\text{tr}} = 1/(2^* \pi^* f_{\text{IMVS}})$ (Fig. S16) [60]. Finally, the target device shows a higher η_{cc} of 83.0% than the control device (54.4%). The conductivity of unmodified and modified SnO_2 films was evaluated by measuring the Hall effect. As a result, SnO_2 films modified with EPN (4.24×10^{-4} S/cm) exhibit higher conductivity than pure SnO_2 (3.37×10^{-4} S/cm), which could be related to the effective passivation of oxygen vacancy defects in SnO_2 films. In conclusion, the device charge transfer and collection became better by EPN modification due to the greater carrier migration driving force and better matching of energy levels.

In addition, nonradiative interface recombination was studied. Transient photovoltage (TPV) was carried out first to study nonradiative recombination. As shown in Fig. 4d, the recombination time increased from 15.83 μs for the control device to 26.17 μs for the target film. Longer recombination time means nonradiative recombination is suppressed when EPN is introduced into the interface. The ideality factor (m) was also extensively proposed to evaluate the recombination in PSCs reliably. As shown in Fig. 4e, the control device with an m of 1.66 while the target is 1.29 indicates that EPN modification can effectively suppress nonradiative recombination, consistent with the TPV results [61,62]. The dark electrochemical impedance spectroscopy (EIS) technique has been widely used to characterize interfacial recombination by evaluating the recombination resistance (R_{rec}). Fig. 4f exhibits the Nyquist plots of the devices based on SnO_2 and EPN-modified SnO_2 , which was measured at a bias of open-circuit voltage (V_{OC}) under dark conditions. An obvious semicircle can be seen and assigned to the R_{rec} . Table S3 shows a significant increase in semicircle radius for devices with structure ITO/ SnO_2 /EPN/perovskite/spiro-OMeTAD/Ag compared with the structure without EPN, suggesting that the R_{rec} of the target device is larger than the control one. A larger R_{rec} means that nonradiative recombination is more difficult to occur. The reduced nonradiative recombination can be attributed to improved interface contact, improved film quality, and more matching energy level arrangement, which reduces defect-assisted nonradiative recombination due to the lack of recombination sites.

Reduced film defect density, improved carrier transport, and suppressed nonradiative recombination lead us to investigate further the effect of the EPN modification on the device. Different concentrations of EPN with the structure of ITO/ SnO_2 /(EPN)/

$\text{Rb}_{0.02}(\text{FA}_{0.95}\text{Cs}_{0.05})_{0.98}\text{PbI}_{2.91}\text{Br}_{0.03}\text{Cl}_{0.06}$ /spiro-OMeTAD/Ag was fabricated to find the best concentration. Fig. 5a and Fig. S17 are the photovoltaic performances with different concentrations of EPN modification. It is clear that all photovoltaic parameters increase with the increasing concentration of EPN. And the champion photovoltaic parameters are obtained when the concentration of EPN is 0.5 mg/mL. Compared with the control device, the target device (0.5 mg/mL) shows a higher short-circuit current density (J_{SC}), which can own to the reduced series resistance (as shown in the EIS) and slightly enhanced UV-vis absorbance. In addition, improved fill factor (FF) and V_{OC} of the control device mainly due to optimized perovskite film quality, reduced film defect density, and nonradiative recombination. Fig. 5b shows the typical J-V curves of the best-performing control and target devices. The champion control device has a J_{SC} of 23.52 and 23.97 mA/cm², a V_{OC} of 1.075 and 1.085 V, an FF of 0.773 and 0.785, and a PCE of 19.54% and 20.42%, reverse scan (RS) and forward scan (FS), respectively. While the target device shows a J_{SC} of 24.58 and 24.32 mA/cm², a V_{OC} of 1.152 and 1.125 V, an FF of 0.818 and 0.814, and a PCE of 23.16 % and 22.27 %, reverse scan (RS) and forward scan (FS), respectively. Devices of photovoltaic performance modified by different molecule modifications (Fig. S18) were carried out to prove the EPN is more competitive (whether multiple-active-site passivation or long chain release stress). The results suggest that the EPN still shows the best performance compared with other molecule-modified PSCs. As shown in Fig. S19 and Fig. S20, the DFT result expresses that although all reference molecules show the charge transfer after contact with SnO_2 or perovskite, the NB and 4NBL do not show an obvious multifunctional passivation effect. Moreover, the binding energy of pDL contracts with SnO_2 or perovskite is also less than the EPN. This result again demonstrates the strength of EPN in indiscriminate multi-site passivation and stress relief. Fig. 5c shows the incident photon-current conversion efficiency (IPCE) spectra of the control and target device. The integrated current density according to the IPCE was estimated to be 23.68 mA/cm² for bare devices and 24.21 mA/cm² for the target device, which were in excellent agreement with the J_{SC} from J-V curves. It needs to be noted that the peak shape of IPCE curves was changed after EPN modification. Since the thickness of perovskite films is the same in our work, we inferred that other factors also would affect the peak shape of IPCE curves except for film thickness. We speculated from experimental results in this work that improved carrier extraction and suppressed interfacial nonradiative recombination should be mainly responsible for the changed peak shape of IPCE curves. Finally, the hysteresis index (HI) was calculated by the formula of $\text{HI} = (\text{PCE}_{\text{RS}} - \text{PCE}_{\text{FS}})/\text{PCE}_{\text{RS}}$, where PCE_{RS} and PCE_{FS} represent the PCE in the reverse scan and the forward scan, respectively. As shown in Fig. S21, the average HI was substantially reduced after EPN modification.

As one of the criteria for commercialization, the stability of the device is also essential. Here, the unencapsulated devices' light, moisture, and thermal without and with EPN modification were measured and compared systematically. For the light stability test, we placed the device with or without EPN modification under standard one sunlight for 250 h. As shown in Fig. 5d, the device with EPN retained 99% of its initial PCE, while 78% of the control device was under the same condition. This result indicates that the device's light stability improved after EPN modification. Fig. 5e is the humidity stability test. We placed the unencapsulated device in an environmental condition with 50–60% relative humidity for tracking tests. The control device only maintained 20% of its initial PCE after aging for 1000 h, while the target device retained 62% of its original PCE. Finally, thermal stability was tested by placing the device on a hot stage at 75 °C in a nitrogen glove box. As exhibited in Fig. 5f, after 1000 h of thermal aging, the control device retained 50% of the original efficiency, while the target device maintained 78% of the original efficiency. In conclusion, the devices modified by EPN exhibited attractive stability. This improved stability can be attributed to 1, improved film quality. It is reported that the improved film quality can reduce the attack sites of water and oxygen [27,56],

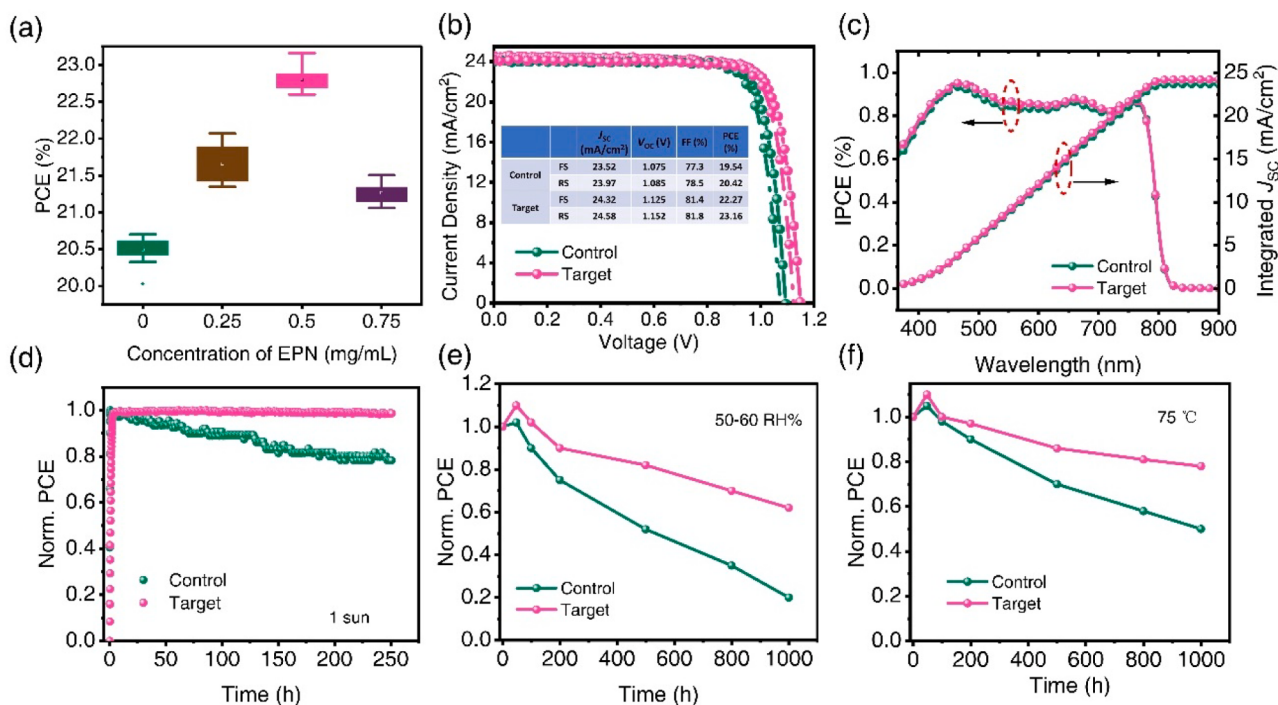


Fig. 5. (a) Statistical distribution diagram of PCE for different concentrations of EPN modification. (b) J - V curves and (c) IPCE of the champion device with or without EPN modified. (d) Light stability, (e) Humidity stability, and (f) thermal stability test of the unencapsulated device without and with EPN modification.

thereby improving the stability of the device. EPN with multifunctional groups (-C = O, -NOO, and -O-) can simultaneously passivate oxygen vacancies in SnO_2 and undercoordinated Pb in perovskite. 2, Released interfacial stress due to the long chain length of EPN [56], which has been widely proven that great stress causes cracks in the device, and this crack can accelerate the failure of the device. 3, Enhanced interface contact. Both the experimental and DFT results reveal that when EPN is introduced at the interface, EPN can form a strong chemical interaction with SnO_2 and perovskite film, which makes EPN act as a bridge to tightly connect SnO_2 and perovskite film, thereby enhancing the interface contact.

3. Conclusions

In conclusion, a new interface buffer layer (EPN) has successfully modified the interface between SnO_2 and the perovskite layer. The experimental results show that after the introduction of EPN, the quality of the film has significantly improved. In addition, the stress of the perovskite film is released due to the change of the substrate. On the other hand, introducing EPN reduces the interfacial nonradiative recombination of the device and obtains a more reasonable energy level arrangement. Finally, SnO_2 /EPN-based PSCs achieved a high PCE of 23.16%. Furthermore, the stability of the device has also been significantly improved, and the unencapsulated PSCs exhibit attractive stability under light, humidity, and high-temperature conditions. This work reveals a buried interface improvement mechanism with multi-site molecules which can provide valuable guidance for designing more effective molecules to passivate the film defects and reduce the interfacial nonradiative recombination to enhance the performance of PSCs devices toward final commercial application.

4. Experimental section

Materials: Thermo Scientific (tin (IV) oxide, 15% in H_2O colloidal dispersion) provided the SnO_2 colloid precursor. Advanced Electron Technology CO., Ltd. supplied Lead (II) bromide (PbBr_2 , 99.9%),

Formamidine hydroiodide (FAI, 99.9%), bis(trifluoromethane) sulfonimide lithium salt (Li-TFSI, 99%), Spiro-OMeTAD (99.86%), lead (II) iodide (PbI_2 , 99.99%), Cesium iodide (CsI, 99.99%), lead (II) chloride (PbCl_2 , 99.99%) and methylamine hydrochloride (MACl, 99.5%) and 4-*tert*-butyl pyridine (tBP, 99%). Rubidium iodide (RbI) was obtained from Aladdin. Sigma Aldrich provided N, N-dimethylformamide (DMF, 99.8%), dimethyl sulfoxide (DMSO, 99.9%), and chlorobenzene (CB, 99.8%). Ethyl p-nitrobenzoate was brought from Tokyo Chemical Industry Co., Ltd. All chemical reagents were utilized as received without further purification.

Device Fabrication: ITO glasses were ultrasonically cleaned for 15 min with detergent water, water, and ethanol. After being blown dry by nitrogen, the ITO was treated for 25 min with ultraviolet ozone (UV-O₃). The SnO_2 colloidal solution was prepared by combining the SnO_2 solution with deionized water at a volume ratio of 1:3. Diluted SnO_2 colloidal solution was spin-coated on ITO substrates for 30 s at a speed of 3000 r/min, and the SnO_2 film was annealed at 150 °C for 30 min. After cooling to ambient temperature, it was subjected to a 20-minute UV-O₃ treatment. For EPN-treated SnO_2 film, different concentrations of EPN were dissolved in ethanol and stirred for 2 h. Then, the EPN solution was spin-coated on the cooled SnO_2 films at 5000 rpm for 30 s and annealed at 100 °C for 10 min. The substrates were then placed in an argon-filled glovebox for perovskite deposition. Perovskite ($\text{Rb}_{0.02}(\text{FA}_{0.95}\text{Cs}_{0.05})_{0.98}\text{PbI}_{2.91}\text{Br}_{0.03}\text{Cl}_{0.06}$) precursor solution was prepared by dissolving PbI_2 (682.7 mg), PbBr_2 (8.5 mg), RbI (6.6 mg), PbCl_2 (12.7 mg), CsI (19.7 mg), FAI (248.2 mg) and MACl (35 mg, additive) into the DMSO/DMF (1/4, v/v) mixture. The perovskite film was deposited using a sequential spin-coating method at 4000 rpm for 30 s, with 100 μL of CB antisolvent dripped over perovskite films for 15 s before the program was terminated, and the film was subsequently annealed at 130 °C for 30 min. 72.3 mg Spiro-OMeTAD, 28.8 μL 4-*tert*-butyl pyridine (tBP), and 17.5 μL lithium bis(trifluoromethane sulfonyl) imide (Li-TFSI) stock solution (520 mg Li-TFSI in 1 mL acetonitrile) in 1 mL CB were combined to make the Spiro-OMeTAD solution. The hole transport layer was then formed by spin-coating 20 μL of Spiro-OMeTAD solution onto the perovskite films at 4000 rpm for 30 s. Finally, using a

shadow mask, a 100 nm silver counter electrode was thermally evaporated on the top of Spiro-OMeTAD under a vacuum of 1×10^{-4} Pa.

Characterization: Grazing incidence X-ray diffraction (GIXRD) patterns were collected using a PANalytical Empyrean diffractometer equipped with a Cu K α radiation ($\lambda = 1.54056$ Å). J-V curves were measured using solar simulator equipment with a 150 W Xenon lamp and a Keithley 2400 source meter. The effective active area of the device was defined to be 0.1 cm^2 by using a black metal mask. Incident photon-to-current conversion efficiency (IPCE) spectra were recorded using a monochromatic Xenon lamp (Bunkouki CEP-2000SRR). UV-vis absorption was measured on an Agilent 8453 UV-Vis G1103A spectrophotometer. Film morphology observations were performed on SEM (Quattro S). The FTIR spectra were recorded with a Nicolet iS50 Infrared Fourier transform microscope. The photoluminescence (PL) and time-resolved photoluminescence (TRPL) were measured with Jasco FP6500 Spectrofluorometer. The X-ray photoelectron spectrometer (Thermo Fischer, ESCALAB 250Xi) was used in this work. In the analysis room, the vacuum is 8×10^{-10} Pa, the excitation source is Al K α ray ($\hbar\omega = 1486.6$ eV), and the working voltage is 12.5 kV. The charge correction was done according to the Energy standard of C 1 s = 284.80 eV. TPC, TPV, IMPS, IMVS, and built-in potential were carried out via PAIOS in the structure of ITO/SnO₂/EPN/perovskite/Spiro-OMeTAD/Ag, and the results were fitted using the companion software of PAIOS. Calculations were performed within the Density Functional (DFT) formalism using the Perdew-Burke-Ernzerhof (PBE) GGA exchange-correlation functional [63]. All calculations were performed utilizing the CP2K package [64] within Gaussian-augmented plane waves (GAPW) dual basis set using the molecularly optimized MOLOPT double ζ -valence polarized (MDZVP) basis set implemented in CP2K code which has a very small Basis Set Superposition errors (BSSE) in gas and condensed phases [65]. The grid cutoff was 450 Ry. The structural minimization was performed with the help of the Broyden-Fletcher-Goldfarb-Shanno algorithm (BFGS).

CRediT authorship contribution statement

H. Bi and P.Y. Su conceived the idea and designed the experiments. H. Bi, L. Liu, and W.B. Shi supervised the research; H. Bi and G.Z. Wang designed the DFT; H. Bi, P.Y. Su, D. Ran, L. Liu, W.J. Hou, and W.B. Shi analyzed the data; H. Bi wrote the paper. All the authors discussed and revised the paper.

Declaration of Competing Interest

The authors declare that they have no known competing financial interests or personal relationships that could have appeared to influence the work reported in this paper.

Data availability

Data will be made available on request.

Acknowledgements

This work was financially supported by the National Natural Science Foundation of China under Grant No. 12104068 and the Natural Science Foundation of Chongqing under Grant No. cstc2021jcyj-msxmX0684, and the Science and Technology Research Program of Chongqing Municipal Education Commission under Grant No. KJQN202201449, the Chongqing Postdoctoral Science Foundation (Grant No. cstb2022nscq-bhx0701), Scientific Research Project of Yangtze Normal University (Grant No. 010730129), and the Doctoral Fund of Southwest University of Science and Technology (no. 21zx7111). The authors are very grateful to Prof. Qing Shen (The University of Electro-Communications) and Prof. Chao Ding (The University of Electro-Communications, Sichuan University) for their meaningful discussions

and assistance with the manuscript. We would like to thank the Analytical and Testing Center of Chongqing University for the XRD measurements (Hanjun Zou).

Appendix A. Supplementary data

Supplementary data to this article can be found online at <https://doi.org/10.1016/j.cej.2023.145077>.

References

- [1] J. Park, J. Kim, H.-S. Yun, M.J. Paik, E. Noh, H.J. Mun, M.G. Kim, T.J. Shin, S. I. Seok, Controlled growth of perovskite layers with volatile alkylammonium chlorides, *Nature* 616 (7958) (2023) 724–730.
- [2] A.S.R. Bati, Y.L. Zhong, P.L. Burn, M.K. Nazeruddin, P.E. Shaw, M. Batmunkh, Next-generation applications for integrated perovskite solar cells, *Commun. Mater.* 4 (2023) 2, <https://doi.org/10.1038/s43246-022-00325-4>.
- [3] F.H. Isikgor, S. Zhumagali, L.V.T. Merino, M. De Bastiani, I. McCulloch, S. De Wolf, Molecular engineering of contact interfaces for high-performance perovskite solar cells, *Nat. Rev. Mater.* 8 (2022) 89, <https://doi.org/10.1038/s41578-022-00503-3>.
- [4] S. Ma, G. Yuan, Y. Zhang, N. Yang, Y. Li, Q.i. Chen, Development of encapsulation strategies towards the commercialization of perovskite solar cells, *Energy Environ. Sci.* 15 (1) (2022) 13–55.
- [5] Z.Y. Xu, Q.X. Zhuang, Y.Q. Zhou, S.R. Lu, X.H. Wang, W.S. Cai, Z.G. Zang, Functional Layers of Inverted Flexible Perovskite Solar Cells and Effective Technologies for Device Commercialization, *Small Struct.* 4 (2023) 2200338, <https://doi.org/10.1002/sstr.202200338>.
- [6] W. Liu, H. Raza, X. Hu, S. Liu, Z. Liu, W. Chen, Key bottlenecks and distinct contradictions in fast commercialization of perovskite solar cells, *Mater. Futures* 2 (1) (2023), 012103, <https://doi.org/10.1088/2752-5724/aca35>.
- [7] Z. Yi, B. Xiao, X. Li, Y. Luo, Q. Jiang, J. Yang, Novel dual-modification strategy using Ce-containing compounds toward high-performance flexible perovskite solar cells, *Nano Energy* 109 (2023), 108241, <https://doi.org/10.1016/j.nanoen.2023.108241>.
- [8] Z. Yi, B. Xiao, X. Li, Y. Luo, Q. Jiang, J. Yang, Revealing the interfacial properties of halide ions for efficient and stable flexible perovskite solar cells, *J. Colloid Interface Sci.* 628 (2022) 696, <https://doi.org/10.1016/j.jcis.2022.07.175>.
- [9] S. Wang, L. Tan, J. Zhou, M. Li, X. Zhao, H. Li, W. Tress, L. Ding, M. Graetzel, C. Yi (易陈道), Over 24% efficient MA-free Cs_xFA_{1-x}PbX₃ perovskite solar cells, *Joule* 6 (6) (2022) 1344–1356.
- [10] H. Li, J. Zhou, L. Tan, M. Li, C. Jiang, S. Wang, X. Zhao, Y. Liu, Y.u. Zhang, Y. Ye, W. Tress, C. Yi, Sequential vacuum-evaporated perovskite solar cells with more than 24% efficiency, *Sci. Adv.* 8 (28) (2022).
- [11] H. Zhang, Z. Ren, K. Liu, M. Qin, Z. Wu, D. Shen, Y. Zhang, H.T. Chandran, J. Hao, C.-S. Lee, X. Lu, Z. Zheng, J. Huang, G. Li, Controllable Heterogenous Seeding-Induced Crystallization for High-Efficiency FAPbI₃-Based Perovskite Solar Cells Over 24, *Adv. Mater.* 34 (36) (2022) e2204366, <https://doi.org/10.1002/adma.202204366>.
- [12] W. Fan, Y. Shen, K. Deng, Q. Chen, Y. Bai, L. Li, Synergistic bonding stabilized interface for perovskite solar cells with over 24% efficiency, *Nano Energy* 100 (2022), 107518, <https://doi.org/10.1016/j.nanoen.2022.107518>.
- [13] R. Sun, Q. Tian, M. Li, H. Wang, J. Chang, W. Xu, Z. Li, Y. Pan, F. Wang, T. Qin, Over 24% Efficient Poly(vinylidene fluoride) (PVDF)-Coordinated Perovskite Solar Cells with a Photovoltage up to 1.22 V, *Adv. Funct. Mater.* 33 (6) (2023) 2210071.
- [14] X. Yue, X. Zhao, B. Fan, Y. Yang, L. Yan, S. Qu, H. Huang, Q. Zhang, H. Yan, P. Cui, J. Ji, J. Ma, M. Li, Surface Regulation through Dipolar Molecule Boosting the Efficiency of Mixed 2D/3D Perovskite Solar Cell to 24%, *Adv. Funct. Mater.* 33 (2022) 2209921, <https://doi.org/10.1002/adfm.202209921>.
- [15] H. Wang, Z. Yang, W. Guo, Y. Ji, Y. Zhou, J. Dang, M. Wang, Functional molecule modified SnO₂ nanocrystal films toward efficient and moisture-stable perovskite solar cells, *J. Alloys Compd.* 890 (2022), 161912, <https://doi.org/10.1016/j.jallcom.2021.161912>.
- [16] H.R. Ma, M.H. Wang, Y.D. Wang, Q.S. Dong, J. Liu, Y.F. Yin, J. Zhang, M.Z. Pei, L. H. Zhang, W.X. Cai, L. Shi, W.M. Tian, S.Y. Jin, J.M. Bian, Y.T. Shi, Asymmetric organic diammmonium salt buried in SnO₂ layer enables fast carrier transfer and interfacial defects passivation for efficient perovskite solar cells, *Chem. Eng. J.* 442 (2022), 136291, <https://doi.org/10.1016/j.cej.2022.136291>.
- [17] S.M. Huang, P.Y. Li, J. Wang, J.C.C. Huang, Q.F. Xue, N.Q. Fu, Modification of SnO₂ electron transport Layer: Brilliant strategies to make perovskite solar cells stronger, *Chem. Eng. J.* 439 (2022), 135687, <https://doi.org/10.1016/j.cej.2022.135687>.
- [18] R. Wang, J. Wu, S. Wei, J. Zhu, M. Guo, Q. Zheng, M. Wei, S. Cheng, Gadolinium-doped SnO₂ electron transfer layer for highly efficient planar perovskite solar cells, *J. Power Sour.* 544 (2022), 231870, <https://doi.org/10.1016/j.jpowsour.2022.231870>.
- [19] C.Y. Wang, J.H. Wu, X.P. Liu, S.B. Wang, Z.L. Yan, L.Q. Chen, G.D. Li, X.P. Zhang, W.H. Sun, Z. Lan, High-effective SnO₂-based perovskite solar cells by multifunctional molecular additive engineering, *J. Alloys Compd.* 886 (2021), 161352, <https://doi.org/10.1016/j.jallcom.2021.161352>.
- [20] P. Xu, H. He, J. Ding, P. Wang, H. Piao, J. Bao, W. Zhang, X. Wu, L. Xu, P. Lin, X. Yu, C. Cui, Simultaneous Passivation of the SnO₂/Perovskite Interface and Perovskite Absorber Layer in Perovskite Solar Cells Using KF Surface Treatment, *ACS Appl. Energy Mater.* 4 (10) (2021) 10921–10930.

- [21] Y. Ming, Y. Zhu, Y. Chen, B. Jin, C. Duan, Z. Liang, L. Zhao, S. Wang, B. Dong, H. Li, C. Wu, beta-Alanine-Anchored SnO₂ Inducing Facet Orientation for High-Efficiency Perovskite Solar Cells, *ACS Appl. Mater. Interfaces* 13 (2021) 57163, <https://doi.org/10.1021/acsami.1c17260>.
- [22] Z. Xiong, X. Chen, B.o. Zhang, G.O. Odunmbaku, Z. Ou, B. Guo, K.e. Yang, Z. Kan, S. Lu, S. Chen, N.A.N. Ouedraogo, Y. Cho, C. Yang, J. Chen, K. Sun, Simultaneous Interfacial Modification and Crystallization Control by Biguanide Hydrochloride for Stable Perovskite Solar Cells with PCE of 24.4%, *Adv. Mater.* 34 (8) (2022) 2106118.
- [23] H. Bi, X. Zuo, B. Liu, D. He, L.e. Bai, W. Wang, X. Li, Z. Xiao, K. Sun, Q. Song, Z. Zang, J. Chen, Multifunctional organic ammonium salt-modified SnO₂nanoparticles toward efficient and stable planar perovskite solar cells, *J. Mater. Chem. A* 9 (7) (2021) 3940–3951.
- [24] Y. Zhong, C. Li, G. Xu, C. Xu, J. Dong, D. Liu, D. Lu, J. You, C. Gao, Q. Song, Collaborative strengthening by multi-functional molecule 3-thiophenboric acid for efficient and stable planar perovskite solar cells, *Chem. Eng. J.* 436 (2022), 135134, <https://doi.org/10.1016/j.cej.2022.135134>.
- [25] H. Bi, G.Y. Han, M.N. Guo, C. Ding, S. Hayase, H.J. Zou, Q. Shen, Y. Guo, W.J. Hou, Top-Contacts-Interface Engineering for High-Performance Perovskite Solar Cell With Reducing Lead Leakage, *Sol. RRL* 6 (2022) 2200352, <https://doi.org/10.1002/solr.202200352>.
- [26] H. Bi, G. Han, M. Guo, C. Ding, H. Zou, Q. Shen, S. Hayase, W. Hou, Multistategy Preparation of Efficient and Stable Environment-Friendly Lead-Based Perovskite Solar Cells, *ACS Appl. Mater. Interfaces* 14 (31) (2022) 35513–35521.
- [27] H. Bi, B.B. Liu, D.M. He, L. Bai, W.Q. Wang, Z.G. Zang, J.Z. Chen, Interfacial defect passivation and stress release by multifunctional KPF₆ modification for planar perovskite solar cells with enhanced efficiency and stability, *Chem. Eng. J.* 418 (2021), 129375, <https://doi.org/10.1016/j.cej.2021.129375>.
- [28] A. Uddin, M. B. Upama, H. Yi, L. Duan, in: *Coatings*, Vol. 9, 2019.
- [29] Z. Yang, B.H. Babu, S. Wu, T. Liu, S. Fang, Z. Xiong, L. Han, W. Chen, Review on Practical Interface Engineering of Perovskite Solar Cells: From Efficiency to Stability, *Sol. RRL* 4 (2020) 1900257, <https://doi.org/10.1002/solr.201900257>.
- [30] Z. Liu, L.K. Ono, Y. Qi, Additives in metal halide perovskite films and their applications in solar cells, *J. Energy Chem.* 46 (2020) 215, <https://doi.org/10.1016/j.jecchem.2019.11.008>.
- [31] P. Liu, N. Han, W. Wang, R. Ran, W. Zhou, Z. Shao, High-Quality Ruddlesden-Popper Perovskite Film Formation for High-Performance Perovskite Solar Cells, *Adv. Mater.* 33 (2021) 20202582, <https://doi.org/10.1002/adma.202002582>.
- [32] K. Liu, Y. Luo, Y. Jin, T. Liu, Y. Liang, L. Yang, P. Song, Z. Liu, C. Tian, L. Xie, Z. Wei, Moisture-triggered fast crystallization enables efficient and stable perovskite solar cells, *Nat. Commun.* 13 (2022) 4891, <https://doi.org/10.1038/s41467-022-32482-y>.
- [33] C. Wang, Y. Zhao, T. Ma, Y. An, R. He, J. Zhu, C. Chen, S. Ren, F. Fu, D. Zhao, X. Li, A universal close-space annealing strategy towards high-quality perovskite absorbers enabling efficient all-perovskite tandem solar cells, *Nat. Energy* 7 (2022) 744, <https://doi.org/10.1038/s41560-022-01076-9>.
- [34] H. Zhong, W. Li, Y. Huang, D. Cao, C. Zhang, H. Bao, Z. Guo, L.i. Wan, X.u. Zhang, X. Zhang, Y. Li, X. Ren, X. Wang, D. Eder, K. Wang, S.F. Liu, S. Wang, All-Inorganic Perovskite Solar Cells with Tetrabutylammonium Acetate as the Buffer Layer between the SnO₂-Electron Transport Film and CsPbI₃, *ACS Appl. Mater. Interfaces* 14 (4) (2022) 5183–5193.
- [35] Z. Shi, D. Zhou, X. Zhuang, S. Liu, R. Sun, W. Xu, L. Liu, H. Song, Light Management through Organic Bulk Heterojunction and Carrier Interfacial Engineering for Perovskite Solar Cells with 23.5% Efficiency, *Adv. Funct. Mater.* 32 (2022) 2203873, <https://doi.org/10.1002/adfm.202203873>.
- [36] H. Bi, Y. Guo, M. Guo, C. Ding, S. Hayase, T. Mou, Q. Shen, G. Han, W. Hou, Highly efficient and low hysteresis methylammonium-free perovskite solar cells based on multifunctional octacetyl potassium interface modification, *Chem. Eng. J.* 439 (2022), 135671, <https://doi.org/10.1016/j.cej.2022.135671>.
- [37] D.B. Khadka, Y. Shirai, M. Yanagida, K. Uto, K. Miyano, Analysis of degradation kinetics of halide perovskite solar cells induced by light and heat stress, *Sol. Energy Mater. Sol. Cells* 246 (2022), 111899, <https://doi.org/10.1016/j.solmat.2022.111899>.
- [38] Z. Zhang, J. Wang, L. Lang, Y. Dong, J. Liang, Y. Zheng, X. Wu, C. Tian, Y. Huang, Z. Zhou, Y. Yang, L. Wang, L. Kong, C.-C. Chen, Size-tunable MoS₂ nanosheets for controlling the crystal morphology and residual stress in sequentially deposited perovskite solar cells with over 22.5% efficiency, *J. Mater. Chem. A* 10 (7) (2022) 3605–3617.
- [39] S.P. Cho, H.J. Lee, Y.H. Seo, S.I. Na, Multifunctional passivation agents for improving efficiency and stability of perovskite solar cells: Synergy of methyl and carbonyl groups, *Appl. Surf. Sci.* 575 (2022), 151740, <https://doi.org/10.1016/j.apsusc.2021.151740>.
- [40] P. Wang, J. Liu, W. Shang, T. Xu, M. Wang, Y. Shi, R. Cai, J. Bian, Rational Selection of the Lewis Base Molecules Targeted for Lead-Based Defects of Perovskite Solar Cells: The Synergetic Co-passivation of Carbonyl and Carboxyl Groups, *J. Phys. Chem. Lett.* 14 (3) (2023) 653–662.
- [41] R. Zhou, X. Liu, H. Li, H. Wang, Y. Ouyang, X. Gong, X. Peng, H. Luo, Y. Ni, W. Zou, Y. Lei, Sulfonyl and Carbonyl Groups in MSTC Effectively Improve the Performance and Stability of Perovskite Solar Cells, *Sol. RRL* 6 (2021) 2100731, <https://doi.org/10.1002/solr.202100731>.
- [42] A. Ioakeimidis, S.A. Choulis, *Materials* 13 (2020) 3289.
- [43] L. Deng, Z. Zhang, Y. Gao, Q. Xiong, Z. Li, J. Xu, Z. Zhang, J. Chen, P. Gao, Electron-deficient 4-nitrophthalonitrile passivated efficient perovskite solar cells with efficiency exceeding 22%, *Sustain. Energy Fuels* 5 (8) (2021) 2347–2353.
- [44] X. Wang, Z. Ying, J. Zheng, X. Li, Z. Zhang, C. Xiao, Y. Chen, M. Wu, Z. Yang, J. Sun, J.R. Xu, J. Sheng, Y. Zeng, X. Yang, G. Xing, J. Ye, Long-chain anionic surfactants enabling stable perovskite/silicon tandems with greatly suppressed stress corrosion, *Nat. Commun.* 14 (2023) 2166, <https://doi.org/10.1038/s41467-023-37877-z>.
- [45] H. Ju, Y.J. Ma, Y. Cao, Z.X. Wang, L.M. Liu, M.X. Wan, T. Mahmoudi, Y.B. Hahn, Y. S. Wang, Y.H. Mai, Roles of Long-Chain Alkylamine Ligands in Triple-Halide Perovskites for Efficient NiO_x-Based Inverted Perovskite Solar Cells, *Sol. RRL* 6 (2022) 2101082, <https://doi.org/10.1002/solr.202101082>.
- [46] S. Liu, X. Guan, W. Xiao, R. Chen, J. Zhou, F. Ren, J. Wang, W. Chen, S. Li, L. Qiu, Y. Zhao, Z. Liu, W. Chen, Effective Passivation with Size-Matched Alkyldiammonium Iodide for High-Performance Inverted Perovskite Solar Cells, *Adv. Funct. Mater.* 32 (2022) 2205009, <https://doi.org/10.1002/adfm.202205009>.
- [47] H. Zhang, W. Yu, J. Guo, C. Xu, Z. Ren, K. Liu, G. Yang, M. Qin, J. Huang, Z. Chen, Q. Liang, D. Shen, Z. Wu, Y. Zhang, H.T. Chandran, J. Hao, Y. Zhu, C.-S. Lee, X. Lu, Z. Zheng, J. Huang, G. Li, Excess PbI₂ Management via Multimode Supramolecular Complex Engineering Enables High-Performance Perovskite Solar Cells, *Adv. Energy Mater.* 12 (2022) 2201663, <https://doi.org/10.1002/aenm.202201663>.
- [48] Z.L. Zhu, N. Li, D.B. Zhao, L.D. Wang, A.K.Y. Jen, Improved Efficiency and Stability of Pb/Sn Binary Perovskite Solar Cells Fabricated by Galvanic Displacement Reaction, *Adv. Energy Mater.* 9 (2019) 1802774, <https://doi.org/10.1002/aenm.201802774>.
- [49] X. Zuo, B. Kim, B.B. Liu, D.M. He, L. Bai, W.Q. Wang, C.Y. Xu, Q.L. Song, C.Y. Jia, Z.G. Zang, D.H. Lee, X. Li, J.Z. Chen, Passivating buried interface via self-assembled novel sulfonium salt toward stable and efficient perovskite solar cells, *Chem. Eng. J.* 431 (2022), 133209, <https://doi.org/10.1016/j.cej.2021.133209>.
- [50] J. Oviedo, M.J. Gillan, Energetics and structure of stoichiometric SnO₂ surfaces studied by first-principles calculations, *Surf. Sci.* 463 (2) (2000) 93–101.
- [51] B. Liu, H. Bi, D. He, L.e. Bai, W. Wang, H. Yuan, Q. Song, P. Su, Z. Zang, T. Zhou, J. Chen, Interfacial Defect Passivation and Stress Release via Multi-Active-Site Ligand Anchoring Enables Efficient and Stable Methylammonium-Free Perovskite Solar Cells, *ACS Energy Lett.* 6 (7) (2021) 2526–2538.
- [52] J. Chen, X. Zhao, S.-G. Kim, N.-G. Park, Multifunctional Chemical Linker Imidazoleacetic Acid Hydrochloride for 21% Efficient and Stable Planar Perovskite Solar Cells, *Adv. Mater.* 31 (39) (2019) 1902902.
- [53] H. Wang, C. Zhu, L. Liu, S. Ma, P. Liu, J. Wu, C. Shi, Q. Du, Y. Hao, S. Xiang, H. Chen, P. Chen, Y. Bai, H. Zhou, Y. Li, Q. Chen, Interfacial Residual Stress Relaxation in Perovskite Solar Cells with Improved Stability, *Adv. Mater.* 31 (2019) 1904408, <https://doi.org/10.1002/adma.201904408>.
- [54] G. Liu, Y. Zhong, H. Mao, J. Yang, R. Dai, X. Hu, Z. Xing, W. Sheng, L. Tan, Y. Chen, Highly efficient and stable ZnO-based MA-free perovskite solar cells via overcoming interfacial mismatch and deprotonation reaction, *Chem. Eng. J.* 431 (2022) 134235.
- [55] N. Yang, C. Zhu, Y. Chen, H. Zai, C. Wang, X.i. Wang, H. Wang, S. Ma, Z. Gao, X. Wang, J. Hong, Y. Bai, H. Zhou, B.-B. Cui, Q.i. Chen, An in situ cross-linked 1D/3D perovskite heterostructure improves the stability of hybrid perovskite solar cells for over 3000 h operation, *Energy Environ. Sci.* 13 (11) (2020) 4344–4352.
- [56] H. Bi, Y. Fujiwara, G. Kapil, D. Tagveniene, Z. Zhang, L. Wang, C. Ding, S. R. Sahamir, A.K. Baranwal, Y. Sanehira, K. Takeshi, G. Shi, T. Bessho, H. Segawa, S. Grigalevicius, Q. Shen, S. Hayase, Perovskite Solar Cells Consisting of PTAA Modified with Monomolecular Layer and Application to All-Perovskite Tandem Solar Cells with Efficiency over 25%, *Adv. Funct. Mater.* 2300089 (2023) <https://doi.org/10.1002/adfm.202300089>.
- [57] L. Wang, B.H. Chang, H. Li, Y.T. Wu, Z. Liu, L. Pan, L. w., Yin,[PbX₆]⁴⁻ modulation and organic spacer construction for stable perovskite solar cells, *Energy Environ. Sci.* 15 (2022) 4470, <https://doi.org/10.1039/d2ee02218d>.
- [58] H.D. Kim, N. Yanagawa, A.i. Shimazaki, M. Endo, A. Wakamiya, H. Ohkita, H. Benten, S. Ito, Origin of Open-Circuit Voltage Loss in Polymer Solar Cells and Perovskite Solar Cells, *ACS Appl. Mater. Interfaces* 9 (23) (2017) 19988–19997.
- [59] D. He, F.W. Zhao, C.R. Wang, Y.Z. Lin, Non-Radiative Recombination Energy Losses in Non-Fullerene Organic Solar Cells, *Adv. Funct. Mater.* 32 (2022) 2111855, <https://doi.org/10.1002/adfm.202111855>.
- [60] M. Chen, M.A. Kamarudin, A.K. Baranwal, G. Kapil, T.S. Ripoll, K. Nishimura, D. Hirotsu, S.R. Sahamir, Z. Zhang, C. Ding, Y. Sanehira, J. Bisquert, Q. Shen, S. Hayase, High-Efficiency Lead-Free Wide Band Gap Perovskite Solar Cells via Guanidinium Bromide Incorporation, *ACS Appl. Energy Mater.* 4 (6) (2021) 5615–5624.
- [61] G.Z. Zhang, J.X. Zhang, Y.Y. Liao, Z.X. Pan, H.S. Rao, X.H. Zhong, Cs₂SnI₆ nanocrystals enhancing hole extraction for efficient carbon-based CsPbI₂Br perovskite solar cells, *Chem. Eng. J.* 440 (2022), 135710, <https://doi.org/10.1016/j.cej.2022.135710>.
- [62] L. Chen, C. Xu, W. Hu, Y. Yao, L. Niu, G. Xu, Y. Zhong, P. Guo, Q. Song, Improving the electrical performance of inverted perovskite solar cell with LiF anode buffer layer, *Org. Electron.* 101 (2022), 106401, <https://doi.org/10.1016/j.orgel.2021.106401>.

- [63] J.P. Perdew, K. Burke, M. Ernzerhof, Generalized Gradient Approximation Made Simple, *Phys. Rev. Lett.* 77 (18) (1996) 3865–3868.
- [64] T. D. Kuhne, M. Iannuzzi, M. Del Ben, V. V. Rybkin, P. Seewald, F. Stein, T. Laino, R. Z. Khalilullin, O. Schutt, F. Schiffmann, D. Golze, J. Wilhelm, S. Chulkov, M. H. Bani-Hashemian, V. Weber, U. Borstnik, M. Taillefumier, A. S. Jakobovits, A. Lazzaro, H. Pabst, T. Muller, R. Schade, M. Guidon, S. Andermatt, N. Holmberg, G. K. Schenter, A. Hehn, A. Bussy, F. Belleflamme, G. Tabacchi, A. Gloss, M. Lass, I. Bethune, C. J. Mundy, C. Plessl, M. Watkins, J. VandeVondele, M. Krack, J. Hutter, CP2K: An electronic structure and molecular dynamics software package - Quickstep: Efficient and accurate electronic structure calculations, *J. Chem. Phys.* 152 (2020), 194103, <https://doi.org/10.1063/5.0007045>.
- [65] T.T. Takaluoma, K. Laasonen, R.S. Laitinen, Molecular dynamics simulation of the solid-state topochemical polymerization of S₂N₂, *Inorg. Chem.* 52 (8) (2013) 4648–4657.